Journal of Electroanalytical Chemistry 932 (2023) 117207

Contents lists available at ScienceDirect

Journal of Electroanalytical Chemistry

journal homepage: www.elsevier.com/locate/jelechem

Effect of tempering temperature and grain refinement induced by severe shot peening on the corrosion behavior of a low alloy steel

L.B. Peral [a,b,*], P. Ebrahimzadeh [a], A. Gutiérrez [c], I. Fernández-Pariente [a]

[a] Department of Material Science and Metallurgical Engineering, Polytechnic School of Engineering of Gijón, University of Oviedo, Spain
[b] Department of Civil Engineering, Structural Integrity Research Group, Higher Polytechnic School, University of Burgos, Spain
[c] Survey and Foresee Technologies S.L. Parque Científico Tecnológico, Ed Polivalente IV. Campus Universitario de Tafira. Las Palmas de Gran Canaria, Spain

ARTICLE INFO

Keywords:
Tempering temperature
Potentyodinamic polarization
Electrochemical impedance spectroscopy
Finite length Warburg
Severe shot peening
Grain refinement

ABSTRACT

In this study, the effect of tempering temperature on the corrosion behavior of a low carbon steel (F1272) was analyzed by means of electrochemical tests: linear polarization resistance, potentyodinamic polarization and electrochemical impedance spectroscopy (EIS) in freely aerated 3.5% NaCl solution, at room temperature. The results show that corrosion resistance of the steel increases with elevating tempering temperature from 200 to 500 °C and finally, to 680 °C. Additionally, a severe shot peening (SSP) treatment was applied in the sample with the best corrosion behavior (TT680), in order to modify the grain structure. Results evidence that corrosion resistance of the TT680 sample decreases after the applied SSP treatment (10A and 5000% coverage). Corrosion behavior is discussed through the different microstructural singularities induced both the heat treatments and the SSP.

1. Introduction

For contributing to the development of the impending new green economy society, based on the use of CO_2-free alternative energy sources, world energy industry must be decarbonized [1,2]. Harnessing the energy resources provided from the marine energy can play an important role in planet decarbonization [3,4]. At this respect, the development of structural steel grades able to work in aggressive marine environments is also a crucial factor.

Although structural steels are frequently used in quenched and tempered condition when a good combination of strength and toughness is required [5,6], other requirements such us corrosion resistance must be addressed. At this respect, steel composition and microstructure are well known to influence corrosion behavior.

In this sense, Katiyar et al. [7] have studied the corrosion behavior in 3.5%NaCl solution of annealed steels with different carbon contents. They reported that corrosion rate increases notably from the ultra-low carbon steel (0.002%C) to the low carbon steel (0.17%C) due to the pearlite appearance. When carbon content increases (i.e. increase in the pearlite content), the cementite to ferrite area ratio in pearlite also increases what contributes to increase corrosion rate [7,8]. Micro-electrochemical cells are produced between Fe_3C that acts as cathode (due to the higher carbon content) and the ferrite matrix, which would act as the anode [9,10]. Nevertheless, the increase in corrosion rate seems to be negligible with the increase in the carbon content from low carbon (0.17%C) to medium (0.43%C) and high carbon (0.7%C). Therefore, although carbon content continues to increase, interlamellar spacing is reduced, contributing now to limit corrosion rate. In this same context, Osorio et al. [11] have also observed that the fine pearlite lamellae, with lower interlamellar spacing, are less sensitive to corrosion in comparison to the coarser pearlite. Regarding the effect of other alloying elements such as Cr, Mo and Ni on the corrosion behavior of high strength low alloy steels, some researchers [12,13] have reported that chromium, molybdenum and nickel promote the formation of compact protective layer, which contributes to improve the corrosion resistance of steel, resulting in a lower corrosion rate.

Katiyar et al. [14] also studied the corrosion behavior, in 3.5% NaCl solution, of a high carbon steel (0.7%C) with five different microstructures. Corrosion behavior was mainly attributed to the shape, size and the distribution of the ferrite and cementite. Steels corrosion resistance decreased according to the following sequence: pearlitic → bainitic → spheroidised → martensitic → tempered martensitic steel. The worst corrosion behavior observed on the martensitic structures might be also adscribed to the higher dislocation level [15]. On the other hand, S. Zhang et al. [16] analyzed the effect of

* Corresponding author.
E-mail addresses: lbperal@ubu.es, luisborja@uniovi.es (L.B. Peral).

https://doi.org/10.1016/j.jelechem.2023.117207
Received 19 July 2022; Received in revised form 19 January 2023; Accepted 26 January 2023
Available online 31 January 2023

three different tempering temperature on the corrosion resistance of a low carbon steel (0.22%C) in artificial seawater. They reported that corrosion resistance can be enhanced by increasing tempering temperature, since increasing tempering temperature, the grain boundary area decreases, contributing to limit the active sites for corrosion attack. At this respect, the grain boundary features should be analyzed to know the contribution of the low and high angle grain boundaries on the corrosion behavior [17].

Additionally, cold plastic deformation, induced by mechanical surface treatments, has been also used to try to improve corrosion resistance. At this regard, mechanical shot peening (SP) treatments can induce grain refinement/nanocrystallization due to the transmitted energy onto the steel surface [18–20] what directly affects corrosion behavior. However, there are conflicting views and theories on the corrosion behavior of the shot-peened layers on the steel surface. After cold-plastic deformation, low angle grain boundaries (LAGBs) and occasionally, high angle grain boundaries (HAGBs) increase [17,21]. Some authors [17,21] have reported that corrosion of the material can mainly occur along HAGBs, whilst low angle grain boundaries (LAGBs) have limited effect on the corrosion behavior [21]. D. Zhang et al. [22] studied the effect of tempered martensite and ferrite/bainite on corrosion resistance of a low alloy steel (API 5L X80 steel). The proportion of high-angle grain boundaries of tempered martensite increased respect to ferrite/bainite steel and consequently, corrosion rate increased from 0.06 mm/year (ferrite/bainite) to 0.11 mm/year (tempered martensite). M. Quiao et al. [23] studied the influence of shot peening on the corrosion behavior of a low alloy steel (0.08% C). They reported that grain refinement, induced by shot peening, improved corrosion resistance. Nevertheless, the influence of the grain boundary features (HAGBs, LAGBs) on corrosion resistance was not reported.

T. Wang et al [24] anlyzed the effect of surface nanocrystallization (grain size 18 nm) induced by shot peening on corrosion resistance of 1Cr18Ni9Ti stainless steel. SP induced a considerably enlarged passive region and raise the breakdown potential of passive film. According to this, some authors [25,26] have reported that nanocrystalline surfaces could increase the density of diffusion paths available for alloying elements to migrate and rapidly form a protective passive layer, what contributes to improve corrosion resistance. Although, HAGBs can increase due to the cold-plastic deformation, the increase in diffusion paths (mainly for Cr in austenitic stainless steel) induced by means of SP can also contribute to balance the negative effect caused by the presence of HAGBs in corrosion resistance. This fact must be addressed depending on the studied steel grade.

On the other hand, A.A. Ahmed et al. [27] indicated a reduction in corrosion resistance after applying SP in an AISI 316L. SP increased corrosion current density from 4.2 to 30.5 $\mu A/cm^2$. At this respect, high-roughness induced by SP increases the practical area for corrosion per unit area. In addition, C. Aparicio et al. [28] revealed that the presence of surface compressive stresses influenced the corrosion behavior of metals after sandblasting. Similar to SP treatments, sandblasting causes more reactive surface, which subsequently decreases the corrosion resistance of metals.

Definitely, although SP treatments might be used to improve corrosion resistance, the mentioned studies evidence that the effect of grain refinement/nanocrystallization induced by SP on corrosion resistance depends on material and its structure. Many parameters such as grain size scale, grain boundary feature, surface roughness, residual stresses or even texture [29,30] play an important role on the corrosion performance.

In this paper, the influence of three different tempering temperatures on the corrosion resistance of an AISI 4340 steel were analysed by means of different electrochemical techniques, in freely aerated 3.5% NaCl solution at room temperature (~22 °C). Besides, in order to study the influence of grain refinement/nanocrystallization on corrosion behavior, a severe shot peening treatment was also applied in the grade with the best corrosion behaviour (TT680 series). Results show that corrosion resistance is directly related to the microstructural singularities and mechanical features.

2. Experimental procedure

2.1. Material and heat treatments

F1272 steel grade, that is a low-alloyed ferritic steel from the Ni-Cr-Mo family, was selected in this study. The chemical composition of the steel, in weight %, is shown in Table 1.

F1272 steel grade was austenitized at 850 °C for 45 min, quenched in water and tempered for two hours at three different temperatures: 200, 500 and 680 °C, respectively. The sequence of heat treatments and the nomenclature of the obtained grades (based on the tempering temperature, TT) are shown in Table 2.

TT680 steel grade, which revealed the best corrosion resistance, was also severely shot peened (SSP) in order to study the impact of grain refinement (induced in the surface layer of the material) on the corrosion behavior. Hence, four different series have been analyzed in this study: TT200, TT500, TT680 (no-peening series) and finally, TT680 + SSP.

2.2. Microstructural characterization

2.2.1. Scanning electron microscopy

Microstructural characterization was carried out by means of a SEM-Jeol-JSM5600 microscope using an acceleration voltage of 20 kV. Previously, the samples were ground and finally polished with diamond paste of 1 μm and etched with Nital-2%.

2.2.2. Hardness analysis

After applying the heat treatments mentioned in Table 2, Brinell Hardness (HB) was measured by means of a Hoytom hardness tester, using a load of 187.5 kg and a ball of 2.5 mm diameter, according to [31]. Three measurements were performed by sample, and the average value was taken.

2.2.3. Phase analysis by X-ray diffraction

In order to quantify phase changes caused by the different treatments, X-ray diffraction analysis was performed on the surface of the steel samples by means of a Seifert XRD 3000 TT diffractometer (Seifert, Massillon, OH, USA).

Parfocal Bragg-Brentano optical configuration was used with a coupled Theta-Theta movement and with the specimen fixed in the center of the goniometer. Furthermore, the radiation is emitted by a thin line molybdenum focus working at 40 kV × 40 mA, and it is then monochromatized to the Kα doublet ($\lambda1$ = 0.7093 Å and $\lambda2$ = 0.7136 Å) by means of a primary filter of zirconium and a secondary monochromator of highly oriented pyrolytic graphite (HOPG). Finally, the collimation of radiation is achieved by the following fixed slit set: 1°-divergence, 2°-antichatter, and 0.1 mm-receiving slits. On the other hand, patterns were registered by a scintillation detector (NaI (Tl)) between 7° y 37° in 2 Theta on fixed mode, with steps of 0.02° and 30 s per point. A fraction of present microstructural phases was calculated by means of the analysis of the different diffractograms obtained by X-ray analysis, using Rietveld structural refinement method [32].

2.2.4. Dislocation density estimation by X-ray diffraction

Dislocation density (ρ) was experimentally measured on the TT200, TT500, TT680 and TT680 + SSP series by using the full width half maximum parameter (FWHM), according to the Williamson-Hall method [33]. The measurements were carried out using the X-ray diffractometer Stresstech 3000-G3R, with Chromium Cr K_α radiation

Table 1
Chemical composition (weight %).

Steel grade	Fe	C	Mn	Si	Cr	Mo	Ni	Cu
F1272	balance	0.41	0.71	0.26	0.87	0.24	1.92	0.21

Table 2
Heat treatment sequence applied on cylindrical bars with 16 mm diameter.

Steel grade ID	Heat treatment sequences
TT200	850 °C/45 min + water quenched + 200 °C/2h tempered + air cooling
TT500	850 °C/45 min + water quenched + 500 °C/2h tempered + air cooling
TT680	850 °C/45 min + water quenched + 680 °C/2h tempered + air cooling

at 30 kV and 6.7 mA. To characterize dislocation density, the 'FWHM' parameter was determined in three different 2Θ (°) positions, corresponding to the martensite/ferrite diffraction planes:

$\{211\}_{2\Theta=156.4^\circ}$, $\{200\}_{2\Theta=106.1^\circ}$ and $\{110\}_{2\Theta=69^\circ}$

Experimental data were analyzed using the Williamson-Hall equation (equation (1)) in the diffraction planes (2Θ).

$$FWHM_{corrected}\frac{\cos(\Theta)}{\lambda}=\frac{K_s}{D}+2\varepsilon\frac{sen(\Theta)}{\lambda} \quad (1)$$

where 'k_s' is a shape factor taken equal to 0.9 [34], 'Θ' is the diffraction angle, 'λ' the X-ray wave-length (0.229 nm for Cr), 'D' is the average particle size and '$FWHM_{corrected}$' is the corrected total full width at half maximum. The dislocation density was calculated using the equation (2), where: 'k' is a constant equal to 14.4 [35] for Body Centered Cubic metals, 'b' represents the Burgers vector with b = 0.248 nm [35] and 'ε' can be calculated from the slope of $FWHM_{corrected}\cdot\cos(\Theta)/\lambda$ versus sen (Θ)/λ plot, by equation (1).

$$\rho=k\left(\frac{\varepsilon}{b}\right)^2 \quad (2)$$

The $FWHM_{corrected}$, avoiding the strain induced by fine grain sizes, is calculated according to equation (3). To do this, an estimation of the instrumental broadening ($FWHM_{instrumental}$) must be done to correct the initial width ($FWHM_{measured}$) of the different peaks, in order to avoid the broadening caused by fine grain sizes [36]. '$FWHM_{instrumental}$' was determined in a sample with a large grain size. Consequently, a sample of the F1272 steel grade was austenitized at 850 °C for 45 min and then, it was slowly cooled into the furnace.

$$FWHM^2_{corrected}=FWHM^2_{measured}-FWHM^2_{instrumental} \quad (3)$$

2.3. Roughness

Surface roughness measurements were performed on all the series, using a Diavite DH-6 roughness tester. Measurements were done in three random positions and directions over a length of 5.6 mm using a cut-off length of 0.8 mm following the UNE EN ISO 4287 standard [37].

2.4. Corrosion analysis

In order to study the corrosion behavior of the mentioned series, linear polarization resistance measurements, potentyodinamic polarization tests and electrochemical impedance spectroscopy (EIS) measurements were performed in freely aerated 3.5% NaCl (with pH 6.6 ± 0.2) solution at room temperature (~22 °C).

Initially, for electrochemical measurements, all the specimens (TT200, TT500 and TT680) were polished using silicon carbide paper up to 1200 grit size. After this, samples were cleaned in an ultrasonic bath for five minutes with isopropyl alcohol and dried in air.

In a second batch, the SSP treated series (TT680 + SSP) was also carefully polished (only with 1200 SiC paper) to remove the highest peaks on the surface of the samples, in order to attain a similar surface roughness to that obtained in the no-peened series (TT200, TT500 and TT680), Table 9. In this way, it is possible to evaluate the microstructural influence on the corrosion behaviour, avoiding the surface roughness interference. Consequently, TT680 + SSP samples were cleaned in an ultrasonic bath for ten minutes, also with isopropyl alcohol, to remove contaminant particles from the severe shot peening and polishing process.

Once samples were prepared and before starting the electrochemical measurements, the open circuit potentials (OCPs) were monitored for one hour until stable OCPs were achieved. In order to ensure reproducibility of results, all the experiments were repeated three times.

All the electrochemical tests were carried out in a flat bottom cell with the help of an IVIUM PocketSTAT potentiostat. The specimens were fitted in the electrochemical cell as working electrode (WE), and platinum mesh was used as a counter electrode (CE). A saturated Ag/AgCl electrode was employed as a reference electrode (RE). A schematic diagram of the electrochemical tests is given in Fig. 1. A circular area of approximately 1.1 cm^2 was exposed to the electrolyte solution.

2.4.1. Linear polarization resistance

The linear polarization (R_p) was conducted at electrode potential ranging ± 0.02 V with respect to OCP at a scan rate of 0.6 V/h [38]. The slope of the overvoltage and current density at corrosion potential provides the value of linear polarization resistance according to equation (4).

$$R_p=\left(\frac{d\,\Delta E}{d\,i}\right)_{i\to0(E=Ecorr)} \quad (4)$$

2.4.2. Potentyodinamic polarization tests

Open circuit potential (OCP) was registered for 1 h on the surface of the different steel series, until attaining potential stabilization. Thereupon, potentyodinamic polarization tests were conducted in the range ± 0.2 V from the OCP at a scan rate of 0.6 V/h [38].

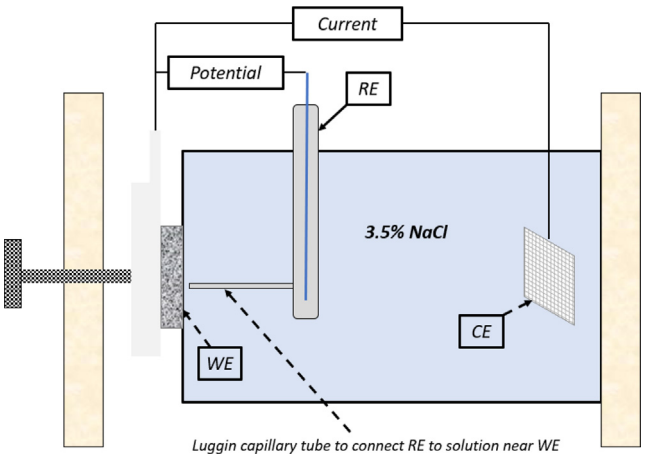

Fig. 1. Schematic diagram of the electrochemical tests.

The polarization curves evidence activation polarization with possibly diffusion-controlled mechanism. Therefore, corrosion is diffusion-controlled where the limiting current density of the oxygen reduction reaction is considered as the corrosion current density in free aerated condition. Oxygen reduction is the main cathodic reaction in freely aerated neutral NaCl solution, $O_2 + 2H_2O + 4e^- = 4\,OH^-$. Hydrogen bubbling was not observed during the polarization tests. As shown later, it seems diffusion that is dominant, on the notion of cathodic Tafel slope is notably greater than the overall Tafel slope (0.12 V/dec) when hydrogen ions are in the activation control. In equation (5), $B_{diff\text{-}control}$ is the Stern-Geary coefficient and β_a represents the anodic slope taken from the potentyodinamic polarization curves. Hence, $B_{diff\text{-}control}$ and the polarization resistance ($R_p \approx R_{Z_w} + R_{ct}$) from the impedance data modelling were used to estimate corrosion current density (i_{corr}) by equation (6) [15,39].

$$B_{diff-control} = \frac{\beta_a}{2.303} \tag{5}$$

$$i_{corr} = \frac{B_{diff-control}}{R_p} \tag{6}$$

Once, corrosion current density (i_{corr}) was calculated, corrosion rate (CR) of the different series was obtained by equation (7), where 'i_{corr}' is the corrosion current density in $\mu A/cm^2$, 'EW' is the equivalent weight of iron considering the oxidation number to be 2 and 'ρ_{steel}' is the density of the steel (7.86 g/cm^3).

$$CR[mm/year] = 3.27 \cdot 10^{-3} \cdot \frac{i_{corr} \cdot EW}{\rho_{steel}} \tag{7}$$

2.4.3. Electrochemical impedance spectroscopy

Initially, the stabilization of open circuit potential (OCP) was performed for 1 h in each series. Then, an electrochemical impedance spectroscopy (EIS) test was carried out in a range of frequency varying from 10^5 to 10^{-2} Hz with ±10 mV (potential amplitude, E_{ac}) sweep from the OCP value [40]. The impedance data were analyzed with the help of Ivium software and fitted to the appropriate equivalent circuit.

2.5. Severe shot peening treatment

Severe plastic deformation methods are well known to be able to induce grain refinement in metallic materials. Severe Shot Peening (SSP) applied with high energy parameters has been recognized to provide notable grain refinement to ultrafine and nano-regime on the surface top layer of the treated samples [18,41,42]. Accordingly, steel series with the best corrosion resistance (TT680 steel in this study) was severely shot peened in order to study the influence of grain refinement on corrosion behavior. In our study, SSP was applied under 5000% coverage to refine the grain structure (Fig. 8d). Therefore, TT680 steel series was shot peened at room temperature in an air blast Shot Peening machine (Guyson Euroblast 4 PF laboratory machine).

Firstly, shot peening treatment was characterized to obtain the Almen intensity according to SAE J443 standard [43]. A plates were shot peened with Z300 shots (Table 5) from different time periods under the conditions listed in Table 3.

Table 3
Almen Intensity characterization on 'A' plates. *Peening flux rate is controlled by means of the peening valve opening in the aforementioned Guyson Euroblast 4PF laboratory machine.

Pressure (bar)	*Peening flux rate	Peening height (mm)	Peening angle (°)
4	2 turns	230	90

The obtained Almen intensity curve is displayed in Fig. 2. Almen intensity corresponds to the Almen saturation point (237 μm). Almen saturation point is related to the arc height that satisfies 'ten percent rule', where the first point of the curve for which doubling the peening time increases the arc height by 10% [43].

Once the Almen intensity was determined, the coverage factor (C) was also estimated by means of the Avrami equation (equation (8)).

$$C\ (\%) = 100 \cdot [1 - \exp(-A_r \cdot t)] \tag{8}$$

here: 'C' represents the coverage factor, 'A_r' is the ratio of total ident area to the target area and 't' is the impact time (in 's'). To estimate '$A_r^{'}$' parameter, a TT680 sample was shot peened for 1 s and the coverage factor (C~ 90%) was obtained by optical analysis (Fig. 3). Once 'A_r' is known ($A_r \sim 2{,}3$), the time necessary to obtain 100% of coverage was obtained by equation (8) (1,70 s). The exposure time for obtaining 5000% coverage was determined multiplying by 50 (Table 4).

2.5.1. Residual stresses and FWHM trend

In order to characterize mechanical features induced by the aforementioned severe shot peening treatment, residual stresses and the full width at half maximum (FWHM) parameter were analysed by means of a Stresstech 3000-G3R X-ray diffractometer. The Kα chromium wavelength (0.2291 nm) was employed onto the {211} ferrite/-martensite planes under a 2Θ angle of 156.4°. The residual stress was determined using the $\sin^2\psi$ technique [44] by means of equation (9).

$$\sigma_{\varnothing} = \left(\frac{E}{1+\nu}\right)_{(hkl)} \left(\frac{1}{d_{\varnothing 0hkl}}\right) \left(\frac{\partial d_{\varnothing\psi hkl}}{\partial \sin^2\psi}\right) \tag{9}$$

where: 'E' and 'v' represent the elastic modulus and Poisson coefficient of the F1272 steel grade in the measured crystallographic plane, taken as 211000 MPa and 0.3, respectively; 'd' is the interplanar distance of the selected diffraction plane (*hkl*), 'ψ' the tilt angle and 'Ø' the angle in the sample plane. The detection of the diffraction peak was carried out at nine positions of the tilt angle, between −45 and +45°, using an exposure time of 40 s in each position. The working parameters used for the measurement of residual stresses are shown in Table 6.

In order to define the in-depth residual stress profiles, thin layers of material were progressively removed by electropolishing, in a Buehler PoliMat machine using a solution of 94% acetic acid and 6% perchloric acid under a voltage of 4 V. The width of the removed layer after each electropolishing stage was measured using a Mitutoyo micrometer, and this procedure was repeated until the residual stress became inexistent.

Additionally, the 'FWHM' parameter (full width at half maximum) of the diffraction peaks was simultaneously measured. This parameter is related to grain distortion, dislocation density, and residual microstrains. The 'FWHM' parameter can be considered as a work hardening index [45].

2.5.2. Microhardness profile

A Vickers microhardness profile was obtained on the cross section of the TT680 + SSP treated sample in order to determine the depth and magnitude of the hardening, due to the plastic deformation induced by SSP treatment (10A and 5000% coverage). Measurements were performed by means of a microhardness tester Buehler Micromet 2100 applying a force of 25 gf during 15 s, following [46]. The measurements were carried out from the sample surface to the core of the sample until attaining hardness stabilization. The diagonals of the indentation marks were measured by optical microscope.

2.5.3. Light mechanical polishing

A slight mechanical polishing process was carefully conducted on the TT680 + SSP samples, by 1200 SiC paper, without altering the

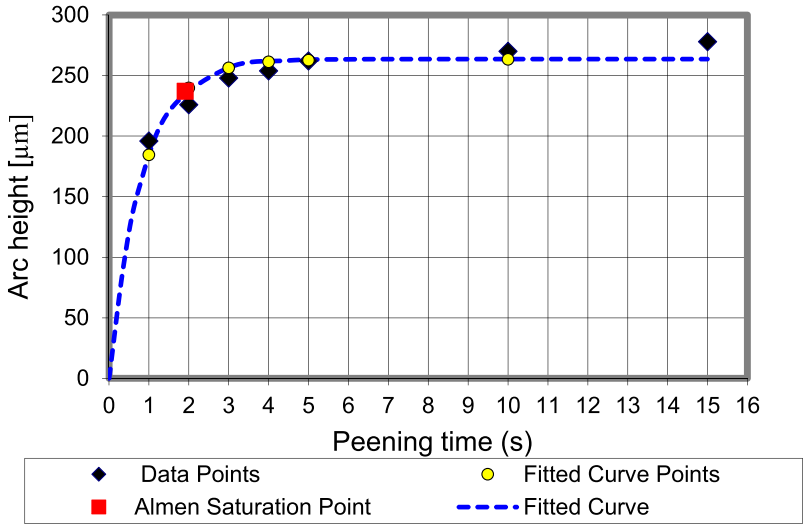

Figure 2. Almen intensity curve on 'A' plates.
Almen saturation point equal to 237 µm or 10A (0,237 mm multiply by 40)

Fig. 2. Almen intensity curve on 'A' plates. Almen saturation point equal to 237 µm or 10A (0,237 mm multiply by 40).

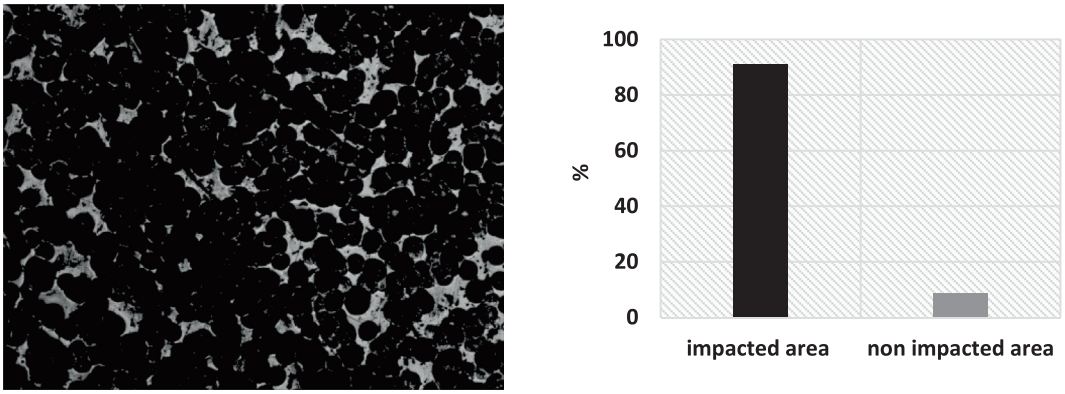

Fig. 3. Coverage factor estimation on TT680 steel series.

Table 4
Shot peening parameters. TT680 steel series.

Almen Intensity	Coverage (%)	Exposure time (s)
10A (237 µm)	5000	85

Table 5
Characteristics of the peening media.

Shot type	Material	Nominal diameter (µm)	Hardness (HV)
Z300	zirconia	300	700

refined surface layer (i.e. grain refinement structure) induced by means of the SSP treatment.

As mentioned above, to analyze the effect of grain refinement (without the surface roughness interference) induced by SSP (10A intensity and 5000% of coverage) on corrosion resistance, surface roughness must be mitigated. At this respect, several studies have reported that corrosion rate increases as surface roughness also increases [19,47].

Table 6
Working parameters used for residual stress measurements.

Measurement mode	Modified χ
Maximum voltage (kV)	30
Exposure time (s)	40
Tilt ψ (°)	9 points between $-45°/+45°$
Noise reduction	Parabolic
Filter of the K_α radiation	Vanadium
Maximum intensity (mA)	6.7
Collimator diameter (mm)	1
Goniometric rotation (measurement direction) Ø (°)	0
Peak adjustment	Pseudo-Voigt

3. Results

3.1. Microstructural analysis and dislocation density estimation

Fig. 4 displays the microstructural observations carried out after the heat treatments described in Table 2. The phase change of the trea-

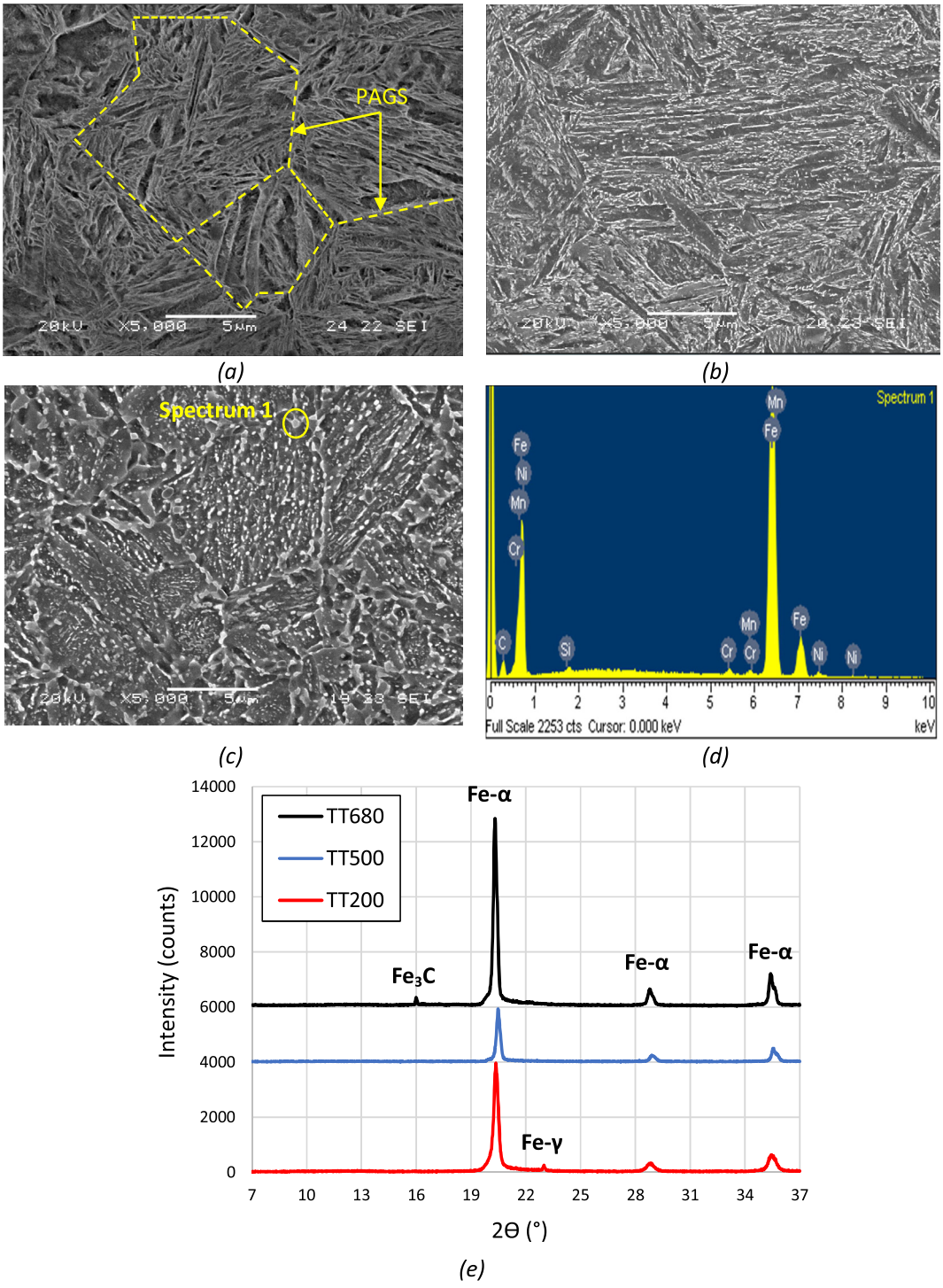

Fig. 4. Microstructures (5000x): (a) TT200, (b) TT500, (c, d) TT680 and (e) XRD patterns of the steel samples.

ted samples was investigated by X-ray diffraction (XRD) analysis (Fig. 4e). The estimated mean prior austenite grain size (PAGS) was around 10 μm.

Series tempered at 200 °C for 2 h (TT200) is mainly composed by lath-like martensite comprising packets, blocks and sub-blocks (Fig. 4a). Retained austenite (approximately 8%) was also identified by means of the XRD analysis (Fig. 4e). Here, carbides precipitation was not observed, presumably due to the low tempering temperature. This series presents high dislocation density level ($\rho = 6{\cdot}10^{10}$ sites/cm^2, Table 7), estimated by means of Williamson-Hall method.

With increasing tempering temperature from 200 °C to 500 °C and 680 °C, microstructure acicularity decreased, dislocation rearrangement/annihilation (Table 7) and substructure recovery takes place [48]. At 500 °C, retained austenite is transformed to lower bainite. It is a heterogeneous mixture composed by supersaturated α solution and Fe carbides (i.e. in this transformation, the residual austenite becomes tempered martensite). TT500 series microstructure corresponds to tempered martensite, which is mainly formed by very small precipitated carbides, embedded in a ferrite matrix (Fig. 4b). Finally, by increasing tempering temperature to 680 °C, profuse carbide pre-

Table 7
Dislocation density estimation according to the Williamson-Hall method.

Steel grade	FWHM$_{corrected}$ (rad) $\{211\}_{156.4°}$	$\{200\}_{106.1°}$	$\{110\}_{69°}$	2ε	R^2	ρ(sites/cm^2)
TT200	0.096	0.032	0.022	0.0031	0.98	$6{\cdot}10^{10}$
TT500	0.043	0.014	0.009	0.0024	0.95	$3{\cdot}10^{10}$
TT680	0.022	0.007	0.005	0.0014	0.90	$1{\cdot}10^{10}$
TT680 + SSP	0.065	0.021	0.014	0.0040	0.94	$9{\cdot}10^{10}$

cipitation (mainly cementite carbides -Fe_3C- identified by EDX analysis in Fig. 4d and XRD analysis in Fig. 4e) can be clearly seen. At this temperature, Fe_3C carbides precipitate, globulize and finally grow to yield a more uniform distribution (Fig. 4c). Here, tempered sample at 680 °C is assumed closer to conventional ferrite and cementite particles than that of martensite. As expected, TT680 series showed the lowest dislocation level ($\rho = 10^{10}$ sites/cm^2, Fig. 5 and Table 7). However, after severe shot peening treatment, dislocation density on the TT680 + SSP series increased to $9{\cdot}10^{10}$ sites/cm^2 (Fig. 5 and Table 7), due to the energy transmitted onto the steel surface.

3.2. Hardness

The aforementioned microstructural differences give rise to the hardness level showed in Fig. 6. In the same figure, the Hollomon-Jaffe parameter (P) evolution is also given depending on the tempering time ('t' in hours) and tempering temperature ('T' in K), according to equation (10).

$$P = T \cdot (20 + \log\ t) \tag{10}$$

Fig. 7 presents the FWHM parameter as a function of the tempering temperature. This parameter is consistent with the hardness measurements. It decreases with increasing tempering temperature and increases after the SSP treatment (TT680 + SSP series) due to the distortion induced in the lattice.

3.3. Severe shot peening

After applying the aforementioned SSP treatment (10A and 5000% coverage) in the TT680 series, residual stresses and FWHM parameter were measured in depth, by means of the XRD technique. To go in-depth, thin layers of the TT680 + SSP samples were progressively removed by an electropolishing method (section 2.5.1). SP treatment induced residual stresses field and work hardening in the upper layer of the material (over 250 μm thickness). Results are respectively shown in Fig. 8a and b.

A microhardness profile was performed in a cross-sectioned sample (Fig. 8c) where SEM observations were also conducted (Fig. 8d). In Fig. 8d, two different areas can be appreciated: the upper layer is characterized by a finer microstructure related to the grain refinement and formation of subgrains induced by the SSP. However, in the inner area, the coarser original microstructure can be observed. In order to determine the grain size (GS) after applying the SSP treatment, the Scherrer's equation [49] (equation (11)) might be used when a nanocrystalline grain size is expected to be obtained [25,42]. Similar SP parameters were previously employed in [18] to obtain a nanocrystalline grain size.

$$GS = \frac{0.9 \cdot \lambda}{FWHM \cdot cos\theta} \tag{11}$$

here: 'λ' is the radiation wavelength (λ chromium = 0.2291 nm) and 'FHHM' is the full width at half maximum. The most intensive first-

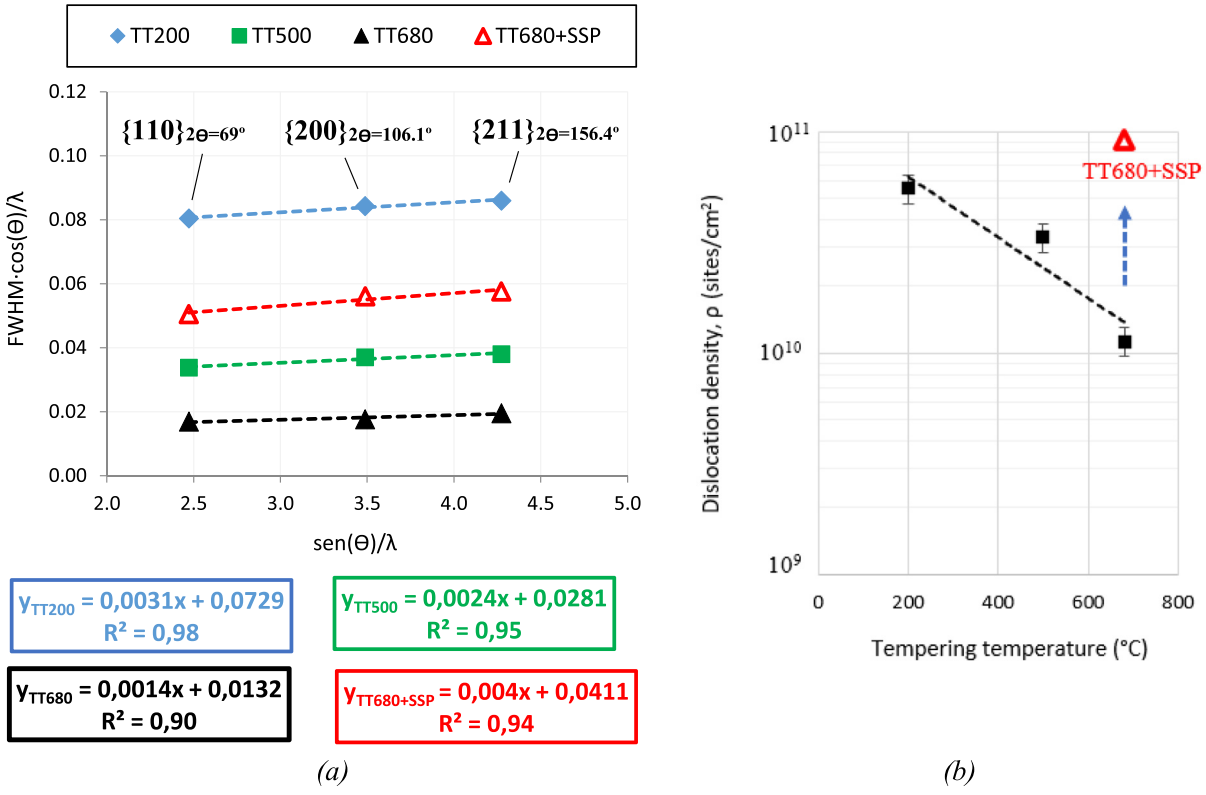

Fig. 5. (a) Dislocation density estimation using the Williamson-Hall method and (b) dislocation density (ρ) evolution versus the tempering temperature (TT).

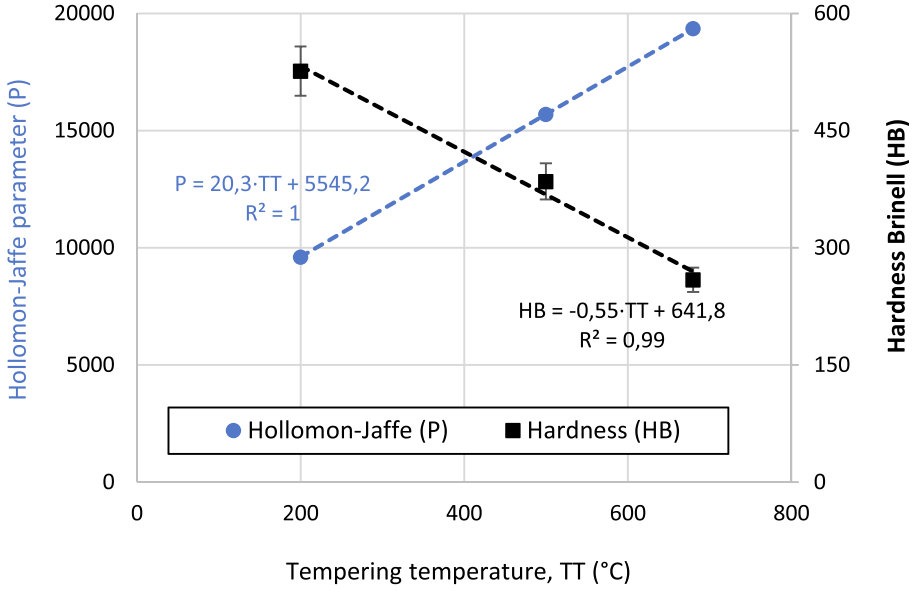

Fig. 6. Hollomon-Jaffe parameter (P) and hardness (HB) trend versus tempering temperature (TT).

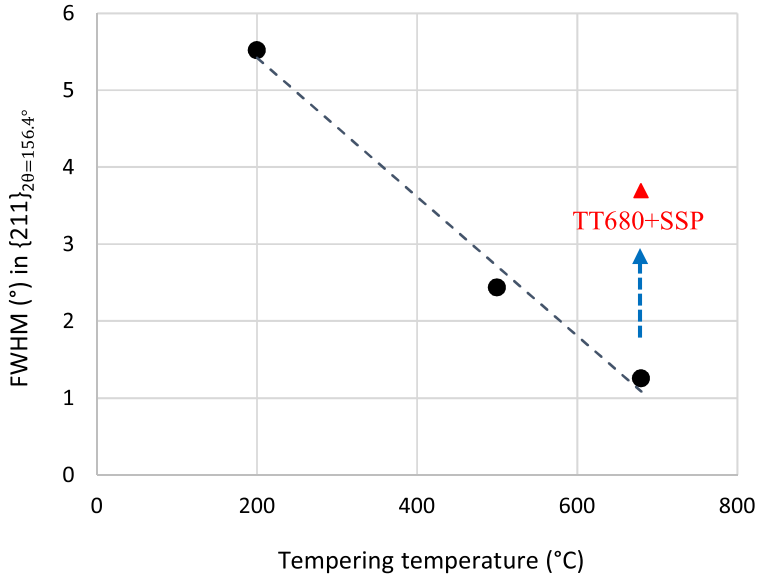

Fig. 7. FWHM parameter trend with tempering temperature (TT).

order peak $\{211\}_{2\theta=156.4^{\circ}}$ of the XRD patterns was taken (0.065 rad in Table 7 for the TT680 + SSP series). 'θ' represents the diffraction angle (θ = 1.36 rad in $\{211\}_{2\theta=156.4^{\circ}}$). Based on these values, a nanocrystalline grain size, in the order of 16 nm, was obtained. The grain size corresponding to the original microstructure (inner part) was analyzed by SEM analysis (10 μm) (Fig. 8d).

On the other hand, shot peening induces high surface roughness level onto the surface of the material. Hence, surface roughness was also characterized. The results, after applying the SSP treatment, are given in Table 8.

It should be recalled that before conducting corrosion analysis, a slight mechanical polishing was carried out in order to reduce the highest roughness peaks, without removing the refined surface layer (Fig. 8d). Despite of this, it is also important to mention that surface grinding involves mechanical deformation and consequently, residual stresses and FWHM parameter were slightly modified (Fig. 9). In this case, to mitigate the surface roughness, 30 μm were approximately removed from the surface of the SSP + TT680 series. Table 9 displays the roughness values determined before conducting the different electrochemical measurements.

3.4. Corrosion analysis

Fig. 10 shows the evolution of the Open Circuit Potential (OCP) as a function of the immersion time in 3.5% of NaCl solution. TT200 series and the severe shot-peened (TT680 + SSP) series exhibited the noblest open circuit potentials, which become more negative with increasing tempering temperature.

With increasing tempering temperature, Cr (0.87%), Mo (0.24%) and Ni (1.92%) can diffuse to carbide precipitation (Fig. 4) and the OCP response becomes more negative what has been also referenced in [15].

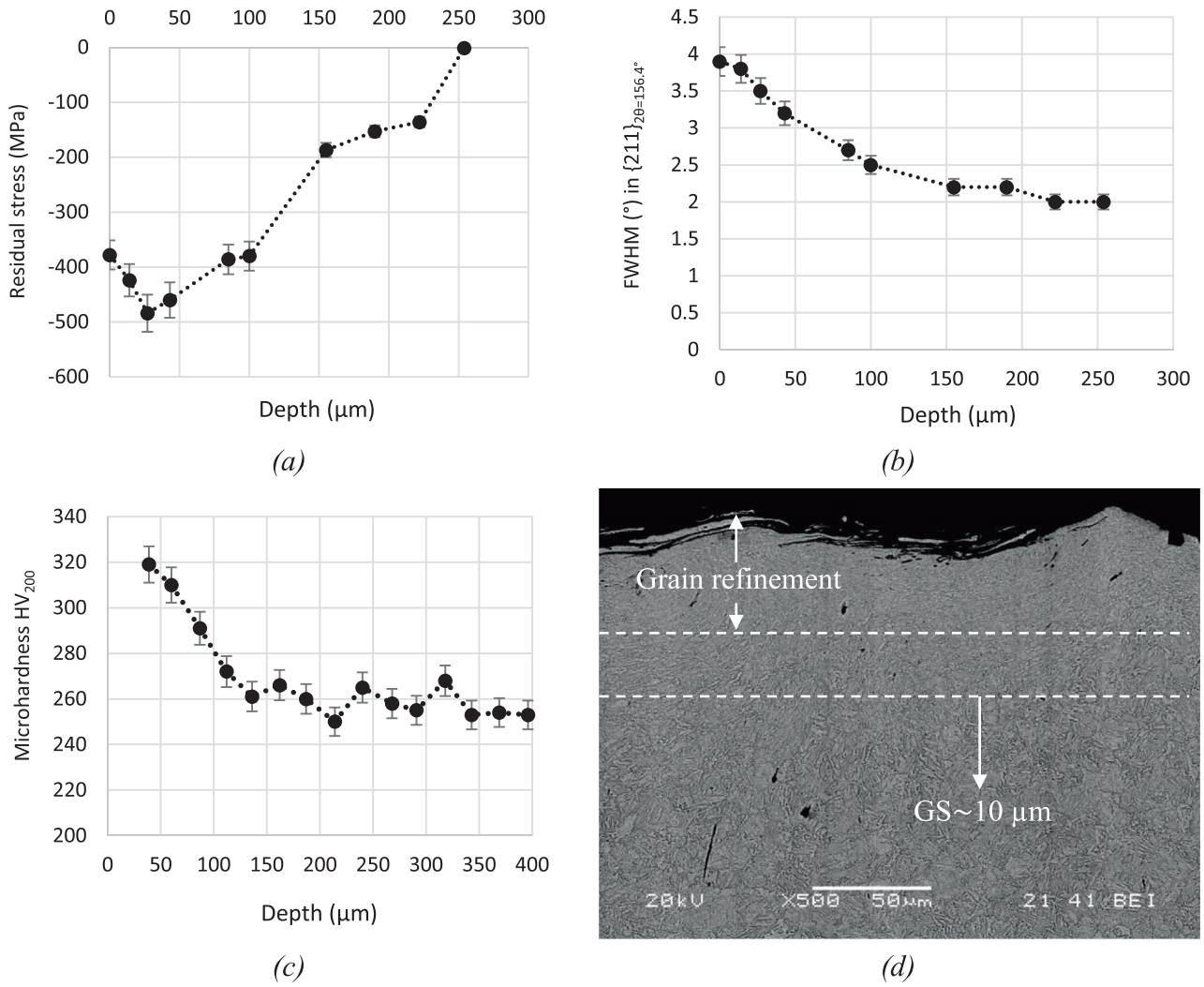

Fig. 8. (a) Residual stress field, (b) FWHM evolution, (c) Microhardness profile and (d) SEM observation of the cross-sectioned sample after severe shot peening treatment (SSP).

Table 8
Roughness parameter after SSP (TT680 + SSP), following UNE EN ISO 4287 standard.

R_a (μm)	R_z (μm)	R_{max} (μm)
4 ± 0.27	20 ± 1.67	26 ± 1.28

3.4.1. Linear polarization resistance (LPR) measurements

Fig. 11 shows the linear LPR curves of all the treated samples. 'R_p' values extracted from the polarization curves analysis are given in Table 10. The results reveal that 'R_p' values of the different series (TT200, TT500 and TT680) increase when tempering temperature also increases. TT680 series has the highest polarization resistance (2221 Ohm, Table 10) among all the other series, and it corroborates well with the lowest corrosion rate obtained by the potentyodinamic polarization method (119 μm/year, Table 11). Nevertheless, polarization resistance decreases to 1505 Ohm after applying the aforementioned SSP treatment on the same steel grade (TT680 + SSP series).

3.4.2. Potentyodinamic polarization tests

Fig. 12 shows the potentyodinamic polarization curves for the different steel series in 3.5% of NaCl solution. Polarization parameters such as the corrosion potential (E_{corr}), corrosion current density (i_{corr}) and anodic slope (β_a) obtained from the analysis of Fig. 12, are displayed in Table 11. On the same table, the $B_{diff\text{-}control}$ parameter (assuming diffusion-controlled cathodic kinetics, equation (5)), the corrosion rate (CR) calculated by equation (7) and the stabilized OCP value (from Fig. 10) are also given.

It is important to note that corrosion rate (i.e. corrosion current density) decreases as tempering temperature increases from 200 to 680 °C (Table 11). The anodic curves are similar and their Tafel slopes span between 60 and 70 mV/dec [15,16]. The cathodic slope of the polarization plots increases gradually (−0.24 V/dec in TT680 to −0.34 V/dec in TT200) with decreasing the tempering temperature (Fig. 12), and it also causes an increase in the corrosion rate. With decreasing the tempering temperature or even, after the peening process, substructure is more stressed and distorted. Therefore, the catalytic activity of the steel surface on enhancing the oxygen reduction reaction is notably associated to the matrix heterogeneity after quenching (mainly in the TT200 series) or after cold-peening (in the case of the TT680 + SSP series). This causes the corrosion rate to increase.

The Tafel slopes, in the cathodic range, are in the order of −0.3 V/dec, clearly above the −0.12 V/dec, what convey that reaction mechanism mainly comes under diffusion control [50,51]. Hence, in our study, we assume corrosion mechanism is under diffusion control ($B_{diff\text{-}control}$, Table 11) of oxygen reduction reaction ($O_2 + 2H_2O + 4e^- = 4OH^-$) and '$i_{corr}$' was calculated by equation (6).

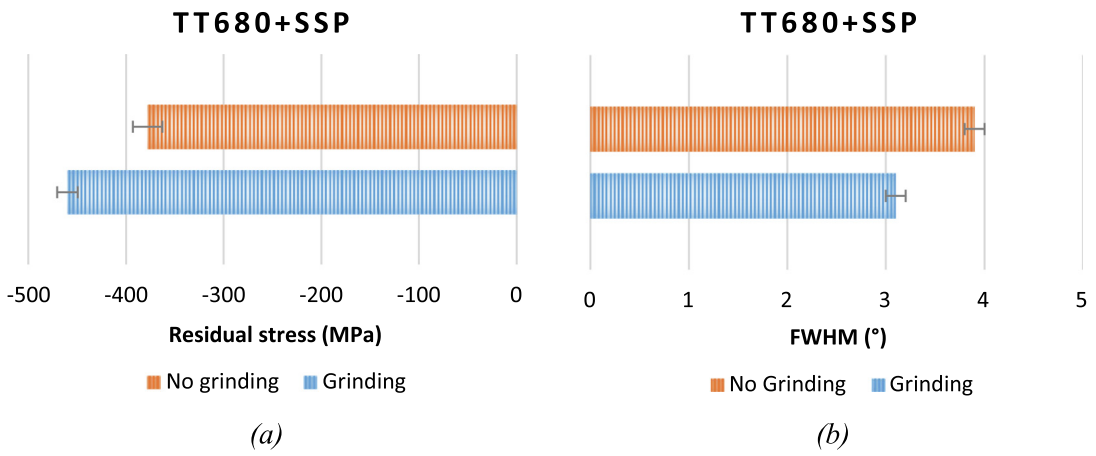

Fig. 9. Effect of grinding (P1200) on residual stresses (a) and FWHM parameter (b).

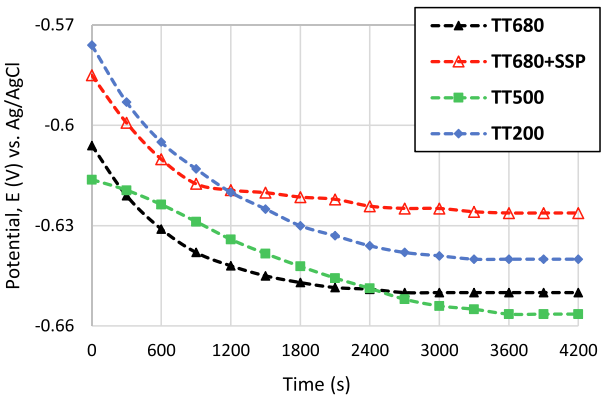

Fig. 10. Evolution of the open circuit potential (OCP) of all series immersed in 3.5% NaCl for 4200 s (T 22 °C and pH 6,6).

Regarding the influence of the SSP treatment on the corrosion resistance, corrosion rate increases to 238 μm/year (TT680 + SSP, Table 11). A similar trend was observed in the evolution of 'R_p'. As expected, the 'R_p' values (Table 10) of the different steel series are observed to be inversely proportional to their corrosion rates (CR).

3.4.3. Electrochemical impedance spectroscopy

In order to confirm the results of the potentyodinamic analysis, electrochemical impedance spectroscopy (EIS) measurements were also carried out. Nyquist plots results are exhibited in Fig. 13a while Fig. 13b and c show the Bode diagrams.

The diameter of the semicircle increases with increasing tempering temperature (Fig. 13a), which implies that the corrosion resistance of the TT680 series is the best among the studied steel series. As shown later by means of the EIS data fitting, polarization resistance ($R_p \approx R_{Ws} + R_{ct}$) decreases in the following order: TT680 > TT500 > TT200 > TT680 + SSP. From Fig. 13b, phase angle maxima oscilates from −66 to −69 deg in the mid-frequency range of the Bode magnitude plots, for all the series. Similar results have been found in [14] for a quenched and tempered microstructure (tempered martensite). In the Bode magnitude plot (Fig. 13c) the impedance modulus |Z| increases with elevating tempering temperature in the low frequency range whilst, it decreases after applying the mentioned SSP.

In a first step, in order to estimate the global corrosion resistance from EIS data, the EIS study was initially limited to a simple resistor–capacitor circuit, Fig. 14. This equivalent circuit was previously proposed in [14,52] to study corrosion behavior of carbon steels in freely aerated 3.5% of NaCl solution. In [14,52], a extensive cathodic

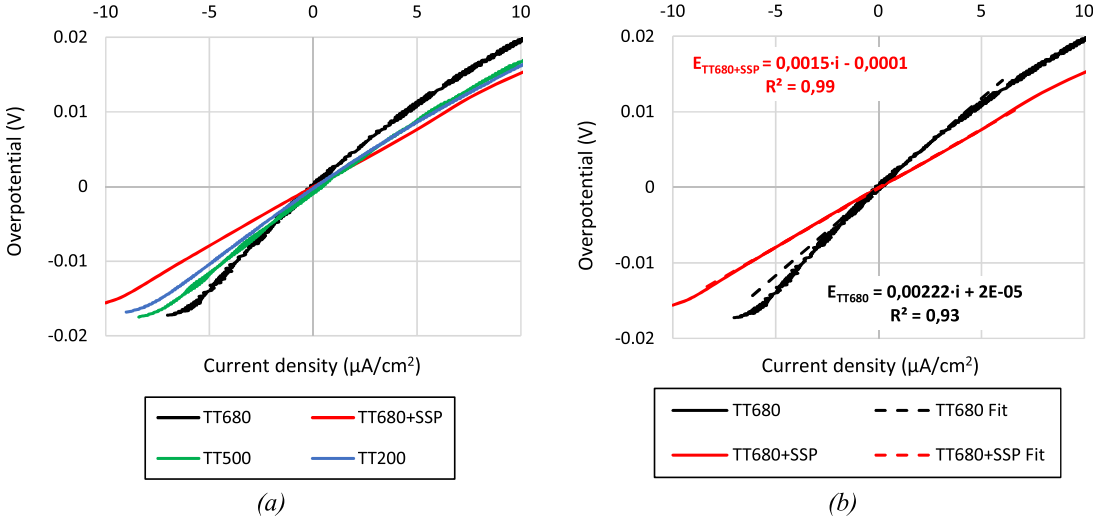

Fig. 11. Linear polarization curves of the samples in 3.5%NaCl. (a) LPR of all the treated samples and (b) LPR results obtained in the TT680 series, with and without SP.

Table 9
Roughness parameters in the different series, following UNE EN ISO 4287 standard.

Sample ID	R_a (μm)	R_z (μm)	R_{max} (μm)
TT200	0.042 ± 0.010	0.39 ± 0.062	0.54 ± 0.092
TT500	0.045 ± 0.005	0.53 ± 0.122	0.66 ± 0.182
TT680	0.048 ± 0.004	0.61 ± 0.082	0.80 ± 0.152
TT680 + SSP	0.075 ± 0.003	1.40 ± 0.017	2.87 ± 0.860

Table 10
Values of the linear polarization resistance (R_p).

Sample	R_p (Ohm)
TT200	1917 ± 88
TT500	2096
TT680	2221 ± 200
TT680 + SSP	1505

scanning was performed, considering the fact that electrochemical event was also under diffusion-controlled mechanism of oxygen reduction reaction. However, and as discussed later, the use of this equivalent circuit might be discussed because of the lack of a diffusion-bounded impedance.

In the equivalent circuit proposed in Fig. 14, 'R_s' is the electrolyte resistance, 'Q_{dl}' represents the constant phase element (CPE) parameters related to the double layer of film electrolyte interface and 'R_{ct}' is the charge transfer resistance. CPE is commonly used to explain the non-ideal capacitance response in the electrochemical process and 'n' is an exponential factor that represents the deviation ($0 < n < 1$) from the ideal capacitance.

The impedance (Z_{CPE}) of a constant phase element is defined by equation (12), where 'Q' is a proportional factor, 'j' represents the complex operator with $j = (-1)^{0.5}$, $w = 2\pi f$ is the angular frequency and 'n' is the aforementioned exponential factor.

$$Z_{CPE} = Q^{-1}(jw)^{-n} \tag{12}$$

The value of 'n' is also associated with the non-uniform distribution of current as a result of the surface defects, microstructure and film formation [53]. According to the 'n' values, mixed behavior between ideal resistor and ideal capacitor is established [14,16]. Electrical parameters, obtained after using the equivalent circuit proposed in Fig. 14, are displayed in Table 12.

The effective interfacial capacitance (C_{eff}, Table 12) can be calculated by equation (13), using 'Q_{dl}', its exponent 'n', and the resistance of solution (R_s) and charge transfer (R_{ct}) as described in [54]. These values are similar to those obtained in [55] where values for interfacial capacitance, varying from 50 to 200 μF/cm^2, are representative of corroding iron surfaces. 'C_{eff}' values, reported in Table 12, are compatible with the observed rough surfaces in Fig. 19. Interfacial capacitance decreases from 233 to 167 μF/cm^2 with increasing tempering temperature. The drop in interfacial capacitance seems to correlate with the increase in the charge transfer resistance, as a result of increasing tempering temperature. This fact was also reported in [15].

$$C_{eff} = Q_{dl}^{1/n} \cdot \left(\frac{1}{R_s} + \frac{1}{R_{ct}}\right)^{(n-1)/n} \tag{13}$$

The equivalent circuit consisting of $R_s(Q_{DL}R_{ct})$ (Fig. 4d) shows good fit for different series having least chi-square (χ^2) value below 0.01. Nevertheless, it seems reasonable to consider a second relaxation (i.e. two time constants) that has not previously been considered in the mentioned equivalent circuit (Fig. 14).

Table 11
Values of OCP and potentyodinamic polarization parameters.

Sample	E_{OCP} (V)	E_{corr} (V)	βa (V/dec)	$B_{diff\text{-}control}$ (V)	i_{corr} (μA/cm^2)	CR (μm/year)
TT200	−0.640	−0.63	0.066	0.029	16	173
TT500	−0.656	−0.65	0.064	0.028	13	141
TT680	−0.650	−0.66	0.061	0.026	11	119
TT680 + SSP	−0.626	−0.62	0.067	0.029	22	238

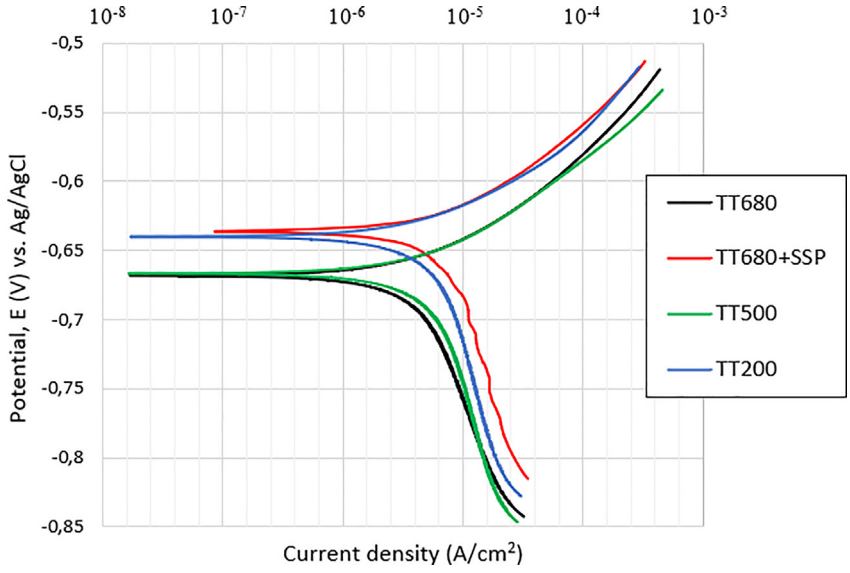

Fig. 12. Potentyodinamic polarization curves of the samples in 3.5%NaCl.

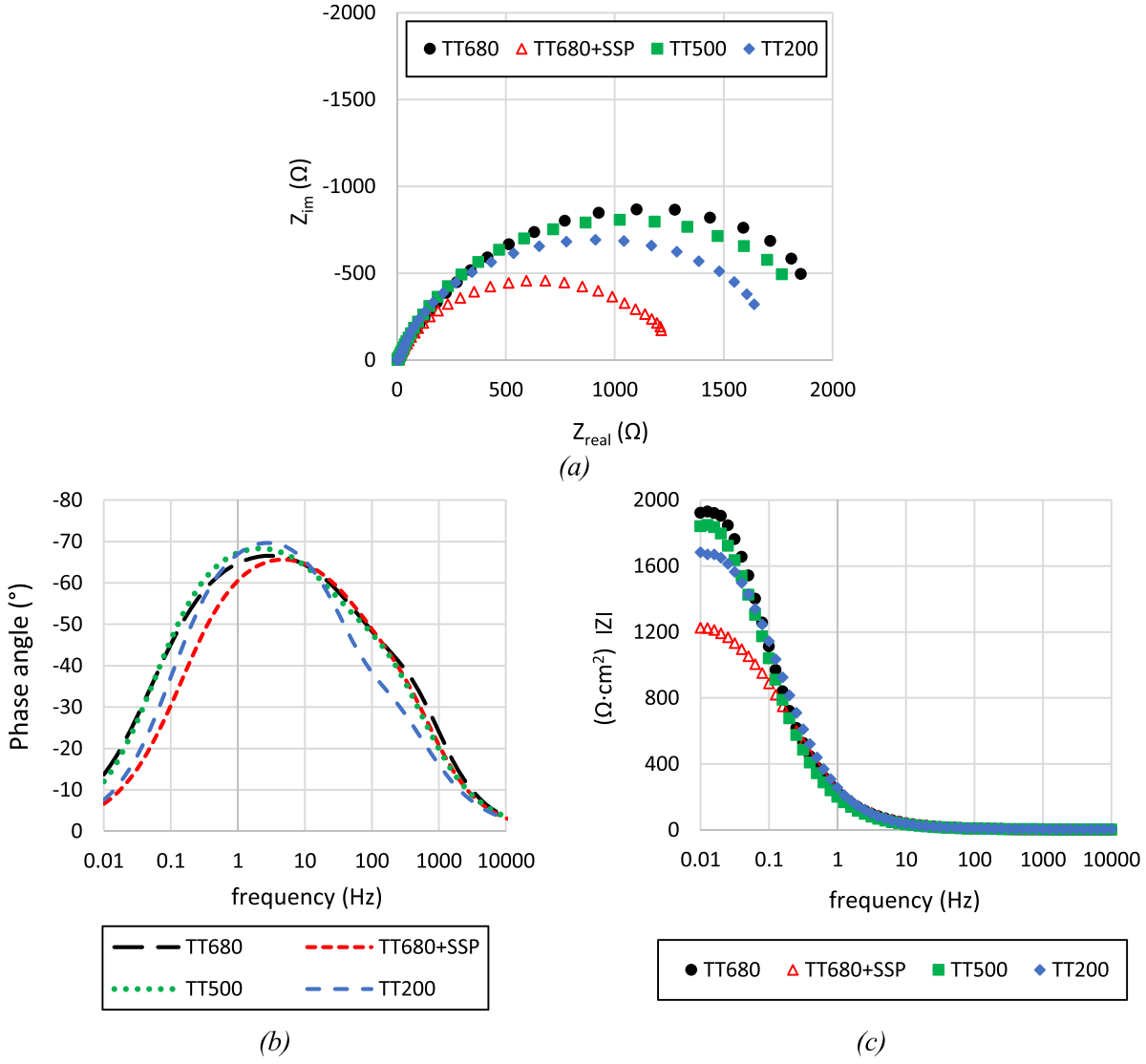

Fig. 13. (a) Nyquist plots, (b) The phase angle-frequency curves and (c) The amplitude-frequency curves for all the series.

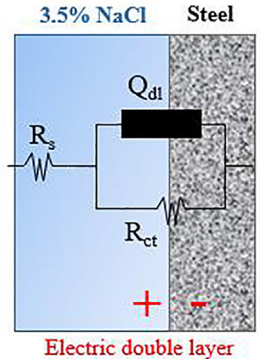

Fig. 14. Resistor-capacitor equivalent circuit.

As mentioned above, through the research work, we have highlighted the cathodic control of the corrosion process (Fig. 12, $\beta_c \gg -0.12$ V/dec). Hence, for a better understanding of the results, in terms of the exposed in the direct current (DC) experiments (diffusion control mechanism, chapter 3.4.2), the presence of a diffusion related impedance should be introduced in the equivalent circuit. The number of time constants can be employed in order to know the number of state variables included in the surface reactions of the corrosion process. From Fig. 13a, two distinct domains seem to be noted. Hence, we propose to use two-time constants; the high-frequency-one associated with the charge transfer resistance and double layer capacitance and the low-frequency-one corresponding to a diffusion-bounded impedance, also known as finite length Warburg (W_s). The impedance parameters are modeled by means of the electrical equivalent circuit proposed now in Fig. 15.

The corroding interface is characterized by a parallel combination of a double layer capacitor Q_{dl} and a finite-length impedance of diffusion, W_s, which represents the cathodic process. The charge transfer resistance is considered small and the system is mainly under mass transport controlled. Analysis of equivalent circuit elements indicates that the contribution of the charge transfer resistance to the impedance of the system is $<5\%$ in comparison to the contribution of the impedance (R_{W_s}) associated with diffusion of cathodic active species. The cathodic process on the steel surface is described by the finite-length Warburg impedance since diffusion of the electrochemically active species (oxygen) is thought to be a limiting stage of the cathodic process. Finite-length Warburg impedance (equation (14)) is characterized by three parameters:

Table 12
The parameters of equivalent circuits for the treated series.

	TT200	TT500	TT680	TT680 + SSP
R_s ($\Omega \cdot cm^2$)	5.3	5.4	5.9	5.0
Q_{dl} ($\Omega^{-1} \cdot cm^2 \cdot s^n$)	$7.0 \cdot 10^{-4}$	$6.0 \cdot 10^{-4}$	$5.0 \cdot 10^{-4}$	$9.8 \cdot 10^{-4}$
n_{dl}	0.84	0.84	0.84	0.8
C_{eff} ($\mu F/cm^2$)	233	203	167	259
R_{ct} ($\Omega \cdot cm^2$)	1788	2036	2146	1297
χ^2(error)	< 0.01	< 0.01	< 0.01	< 0.01

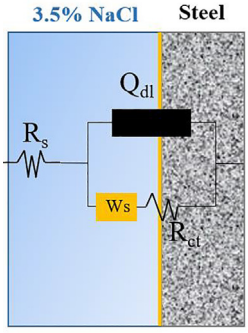

Fig. 15. Equivalent circuit with a short length Warburg (Ws).

R_{W_s}: finite length Warburg diffusion resistance.
τ_{W_s}: the time-constant parameter.
n_{W_s}: the exponential parameter.

$$\hat{Z} = \frac{R_{W_s}}{(i \cdot w \cdot \tau_{W_s})^{n_{W_s}}} \tanh\left((i \cdot w \cdot \tau_{W_s})^{n_{W_s}}\right) \quad (14)$$

The data, which has been extracted from the model proposed in Fig. 15, show an excellent fit ($\chi^2 < 0.002$) with the finite-length Warburg element. Results are listed in Table 13. Nyquist plots and data fitting are shown in Fig. 16. The fitting values of n_{W_s} are in the range of 0.6–0.8 (Table 13). These values are higher than those commonly associated to an usual diffusion impedance. Anyway, the values of n_{W_s} do not strictly adhere to 0.5 to define the diffusion impedance for heterogeneous systems [56].

Additionally, it is important to mention that in the case of the TT680 series, some deviations were evidenced in the data fit, especially, for experimental points at the lower test frequencies (Fig. 16). One of the reasons for this scatter was that the surface scale can change during the EIS measurements and then, affected the low-frequency impedance readings, which take a much longer time to measure. Another possible reason for the low-frequency deviation was the frequency dispersion introduced by Cole et al. [57] which might be caused by variation in surface heterogeneity, scale thickness and roughness. Anyway, data analysis, performed by the circuit proposed in Fig. 15, gave a reasonable estimation of the electrochemical parameters. Besides, the use of this electrical circuit, to fit the EIS data, is in agreement with what was previously evidenced in the direct current (DC) experiments.

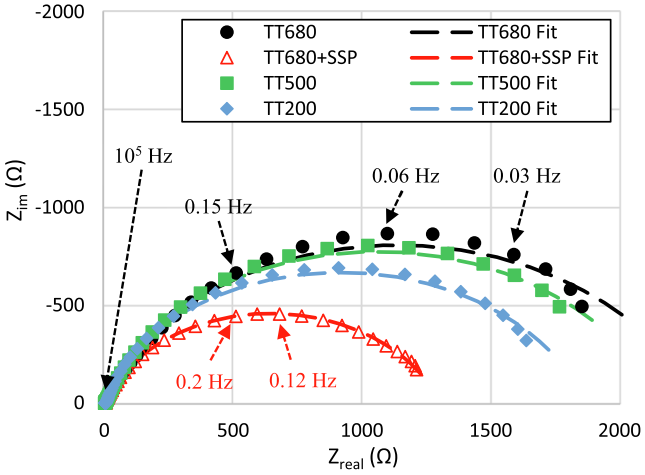

Fig. 16. Data fitting by means of the equivalent circuit proposed in Fig. 15.

Further investigations are needed to orient the choice of the optimal number of time constants, for instance, modifying the stirring rate of the electrolyte. In this case, it would be possible to define more concisely the influence of each relaxation state in the diffusion-controlled cathodic kinetics and/or activation-controlled kinetics. In this study, we have evidenced corrosion process with possibly diffusion-controlled mechanism. Definitely, regarding corrosion rate calculations, a higher capacitive arc diameter implies a lower corrosion rate. The diameter of the semicircle increases by elevating the tempering temperature from 200 to 680 °C (Fig. 13a and Fig. 16) while, it decreases when the SSP was applied to TT680 series (with $R_p \approx R_{W_s} + R_{ct} = 1295$ Ohm). This fact suggests that the corrosion resistance of the TT680 grade (without shot peening) is the best among the steel series (the polarization resistance, $R_p \approx R_{W_s} + R_{ct}$, is biggest for TT680 steel, with $R_p = 2312$ Ohm). Polarization resistance ($R_{W_s} + R_{ct}$) results obtained in the EIS measurements are consistent with those found in the LPR experiments (DC). These results are also aligned with corrosion behavior determined from the potentyodinamic polarization measurements (Fig. 17).

Table 13
The parameters of equivalent circuits for the treated series.

	TT200	TT500	TT680	TT680 + SSP
R_s ($\Omega \cdot cm^2$)	4.3	2.5	2.5	2.9
Q_{dl} ($\Omega^{-1} \cdot cm^2 \cdot s^n$)	$8.2 \cdot 10^{-4}$	$1.0 \cdot 10^{-3}$	$9.3 \cdot 10^{-4}$	$8.7 \cdot 10^{-4}$
n_{dl}	0.78	0.78	0.76	0.77
R_{ct} ($\Omega \cdot cm^2$)	8	12	42	45
R_{W_s} ($\Omega \cdot cm^2$)	1840	2120	2270	1250
τ_{W_s} (s)	0.30	0.53	0.48	0.14
n_{W_s}	0.81	0.70	0.62	0.63
χ^2(error)	$1.3 \cdot 10^{-3}$	$5.6 \cdot 10^{-4}$	$1.1 \cdot 10^{-3}$	$5.6 \cdot 10^{-4}$

4. Discussion

Corrosion resistance is discussed in terms of the different microstructural singularities and mechanical features.

Based on the results, as tempering temperature decreases from 680 to 200 °C corrosion resistance decreases (i.e. corrosion rate increases). Accordingly, with decreasing tempering temperature, the dislocation density increases (Fig. 18). Hence, it is suggested that dislocations are active sites for corrosion [58], what contributes to increase corrosion rate (Fig. 18). A greater plenty of dislocations encourage iron dissolution, via direct oxidation or driven by reduction.

On the other hand, some authors [14,15,59] have reported that ferrite matrix act as anode while the Fe_3C particles would act as the cathode due to its more positive potential than ferrite. Based on this, TT680 grade with higher Fe_3C particles (Fig. 4c, d, e) could be expected, a priori, to exhibit the worst corrosion behavior as more micro-electrochemical cells (ferrite-Fe_3C couple) might exist, in terms of its microstructure. However, the different microstructural singularities seem to play a different competitive role on the corrosion behavior. Although, on the one hand, the increase of the tempering temperature from 200 to 680 °C promotes the precipitation of Fe_3C particles, which might initially contribute to decrease corrosion resistance; on the other hand, with increasing tempering temperature, the lattice distortion released (i.e. FWHM parameter decreases, Fig. 7) and the density of dislocation also decreases (Fig. 5b). These last two effects prevail, contributing to increase corrosion resistance as the tempering temperature increases, regardless of the Fe_3C particles precipitation.

Furthermore, the worst corrosion behavior observed in the TT200 grade, it is not only explained due to its high dislocation level ($6{\cdot}10^{10}$ sites/cm^2) and lattice distortion but also by the formation of the microgalvanic contribution between ferrite/martensite and retained austenite (8%, Fig. 4e), promoting ferrite/martensite dissolution [60].

Additionally, to study the influence of the SP treatment on the corrosion resistance, the TT680 series, that initially had showed the best corrosion resistance, was also severe shot-peened (TT680 + SSP). Plastic deformation, induced by the SSP, results not only in grain refinement and formation of subgrains but also in high dislocation density (Fig. 5b). Hence, dislocations cause highly localized stress, leading to the preferential dissolution of metal atoms. A similar effect was also reported in [15]. In addition, plastic deformation induced by means of the high energy created during the SSP (10A and 5000% coverage) increases the volume fraction of grain boundaries. According to this, it is well known that the grain boundaries are very high energy active sites, which led to the increasing the current density. As a result, the formation of the galvanic couple between the anodic grain boundary and the cathodic interior grain also contribute to increase the corrosion rate. Besides, some authors [28] have also argued that the presence of surface compressive stresses decreases the corrosion resistance of metals because of the induced large density of crystal defects and lattice distortion. In our study, after applying the aforementioned SSP treatment, the FWHM parameter, related to the lattice distortion, notably increased to 4° near the surface layer (Fig. 8b), whilst compressive residual stresses, in the range of −500 MPa (Fig. 8a), were induced. Definitely, these facts contribute to justify the worst corrosion behavior observed in the TT680 + SSP series, when compared to the un-peened TT680 series.

Additionally, SEM observations have been also carried out. A outer rust layer structure, composed of granules of corrosion products (i.e. flaky particles), was observed. In artificial seawater, containing chloride ions, the formation of these corrosion products, including Fe_3O_4 and γ-FeOOH, has been widely reported in the literature [16]. Corrosion products of the outer layer were easily removed with a soft brush and vibration in an ultrasonic bath. After this, different features were noted among the surfaces of the treated series. In the TT680 + SSP series, micro-pits were observed (Fig. 19b and c). The quantity of manganese inside the pits was notably higher than that outside the corrosion pits. This fact is because pitting corrosion, motivated by the SSP treatment (with high energy delivered onto the steel surface), takes place at the manganese inclusions [61,62]. However, pitting corrosion was not observed in the TT680 un-peened series (Fig. 19a).

Despite the different conflicting theories on the corrosion behavior of the shot-peened layers, in this study, the SSP treatment performed under the mentioned conditions has not contributed to increase the corrosion resistance of the studied low carbon steel when grain refinement or even nanocrystalline structures (~16 nm) are created. Never-

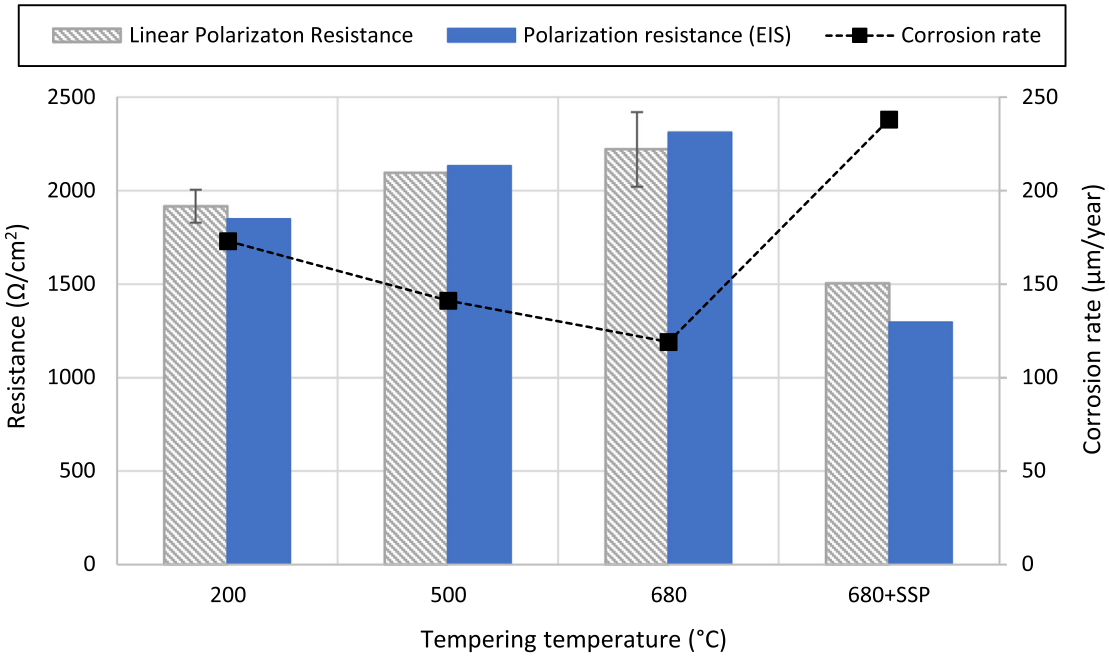

Fig. 17. Electrochemical measurements in 3.5% NaCl. F1272 steel grade. Polarization resistance (EIS) was estimated by means of the circuit provided in Fig. 15.

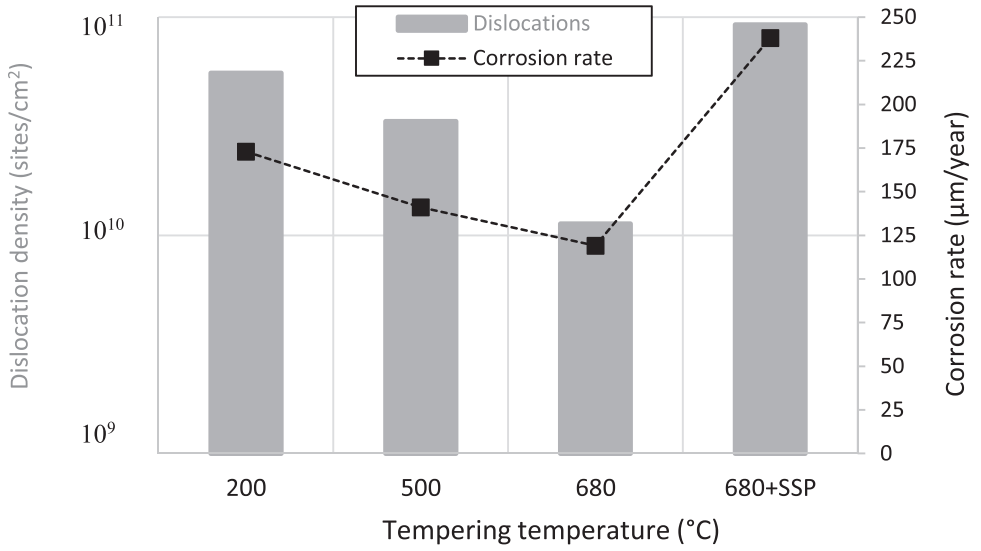

Fig. 18. Dislocation density and corrosion rate evolution depending on the tempering temperature and SSP treatment.

Spectrum a-1 (wt%)					
C	Ni	Cr	Mn	Fe	O
1.00	2.00	0.75	0.85	94.00	1.40

Spectrum b-1 (wt%)					
C	Ni	Cr	S	Mn	Fe
0.80	0.76	1.00	14.00	22.00	61.40

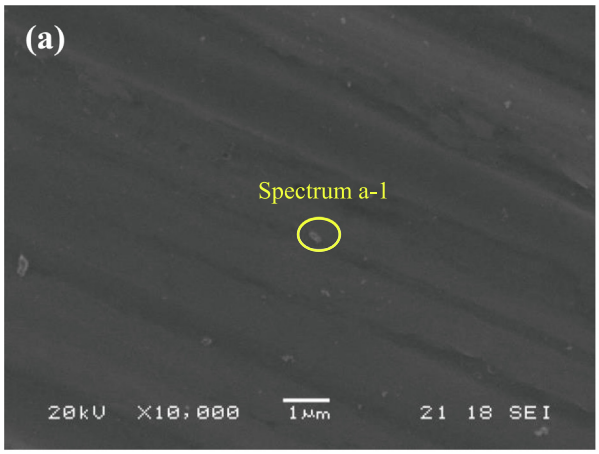

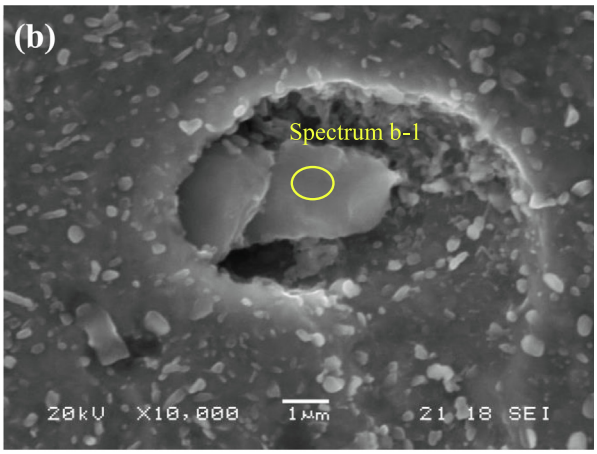

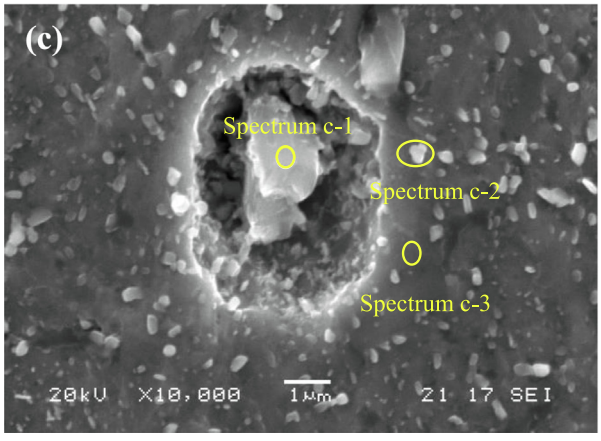

Spectrum c-1 (wt%)				
C	Cr	S	Mn	Fe
0.90	0.86	22.00	35.00	41.20

Spectrum c-2 (wt%)					
C	Ni	Cr	Mn	Fe	O
1.00	1.10	1.70	1.15	93.80	1.25

Spectrum c-3 (wt%)				
C	Ni	Cr	Fe	O
0.80	1.30	0.60	96.30	1.00

Fig. 19. SEM morphologies of the outer layer of the corroded surfaces. (a) TT680 series, (b) and (c) TT680 + SSP series.

theless, by increasing the tempering temperature, the corrosion resistance was considerably improved.

5. Conclusions

The present study has evaluated the corrosion behaviour of three different series (one of them submitted to SP, TT680 + SSP series) of a low carbon steel (F1272) after different tempering treatments (200, 500 and 680 °C for 2 h) in freely aerated 3.5% NaCl solution, by means of different electrochemical techniques.

The results evidence the relationship between tempering temperature and corrosion resistance. Corrosion behaviour improves with increasing tempering temperature. This fact seems to be strongly influenced by the dislocation density (varying from $6{\cdot}10^{10}$ to 10^{10} sites/cm^2 as tempering temperature increases from 200 to 680 °C). The presence of Fe_3C on the microstructure of the TT680 series could suggest the existence of preferred zone for corrosion, but results demonstrate the predominant effect of dislocation density. Corrosion rate decreases in the following order: TT200 (slightly tempered martensite) → TT500 (tempered martensite) → TT680 (highly tempered martensite). This trend corroborates well with the increase in the polarization resistance (R_p) determined from the LPR and EIS measurements.

The severe shot peening treatment (10A and 5000% coverage) performed on the TT680 series induced grain refinement and formation of subgrains (grain size varies from 10 μm in the core to 16 nm near the surface layer). TT680 + SSP series (followed by slight polishing in order to avoid surface roughness effects) showed the lowest corrosion resistance. The increase in the volume of grain boundaries fraction due to the grain refinement, the lattice distortion caused by the induced plasticity and the areas with high level of dislocations ($9{\cdot}10^{10}$ sites/cm^2) seem to interfere the exposed electroactive surface, with higher surface reactivity, encouraging corrosion. In the surface of the TT680 + SSP series, pitting corrosion was observed at the Mn inclusions.

Declaration of Competing Interest

The authors declare that they have no known competing financial interests or personal relationships that could have appeared to influence the work reported in this paper.

Acknowledgments

L.B. Peral is grateful for his Margarita Salas Postdoctoral contract (Ref.: MU-21-UP2021-030) funded by the University of Oviedo through the Next Generation European Union. P. Ebrahimzadeh is also grateful for his Predoctoral contract (Ref.: PAPI-21-PF-21) funded by the University of Oviedo and the Santander Bank.

References

[1] S. Griffiths, B.K. Sovacool, J. Kim, M. Bazilian, J.M. Uratani, Industrial decarbonization via hydrogen: A critical and systematic review of developments, socio-technical systems and policy options, Energy Res. Soc. Sci. 80 (2021), https://doi.org/10.1016/j.erss.2021.102208 102208.

[2] P.K. Singh, H. Chudasama, Conceptualizing and achieving industrial system transition for a dematerialized and decarbonized world, Glob. Environ. Chang. 70 (2021), https://doi.org/10.1016/j.gloenvcha.2021.102349 102349.

[3] D. Gielen, F. Boshell, D. Saygin, M.D. Bazilian, N. Wagner, R. Gorini, The role of renewable energy in the global energy transformation, Energ. Strat. Rev. 24 (2019) 38–50, https://doi.org/10.1016/j.esr.2019.01.006.

[4] M. Grayson, Energy transitions, Nature 551 (2017) S133–S, https://doi.org/10.1038/d41586-017-07507-y.

[5] L.B. Peral, A. Zafra, J. Belzunce, C. Rodríguez, Effects of hydrogen on the fracture toughness of CrMo and CrMoV steels quenched and tempered at different temperatures, Int. J. Hydrogen Energy 44 (2019) 3953–3965, https://doi.org/10.1016/j.ijhydene.2018.12.084.

[6] L.B. Peral, I. Fernández-Pariente, C. Colombo, C. Rodríguez, J. Belzunce, The positive role of nanometric molybdenum-vanadium carbides in mitigating hydrogen embrittlement in structural steels, Materials. 14 (2021) 7269, https://doi.org/10.3390/ma14237269.

[7] P.K. Katiyar, S. Misra, K. Mondal, Effect of different cooling rates on the corrosion behavior of high-carbon pearlitic steel, J. Mater. Eng. Perform. 27 (2018) 1753–1762, https://doi.org/10.1007/s11665-018-3256-3.

[8] F. Sun, X. Li, X. Cheng, Effects of carbon content and microstructure on corrosion property of new developed steels in acidic salt solutions, Acta Metallurgica Sinica (English Letters). 27 (2014) 115–123, https://doi.org/10.1007/s40195-013-0007-1.

[9] J.B. Sun, G.A. Zhang, W. Liu, M.X. Lu, The formation mechanism of corrosion scale and electrochemical characteristic of low alloy steel in carbon dioxide-saturated solution, Corros. Sci. 57 (2012) 131–138, https://doi.org/10.1016/j.corsci.2011.12.025.

[10] W. Liu, H. Zhang, Z. Qu, Y. Zhang, J. Li, Corrosion behavior of the steel used as a huge storage tank in seawater, J. Solid State Electrochem. 14 (2010) 965–973, https://doi.org/10.1007/s10008-009-0886-2.

[11] W.R. Osório, L.C. Peixoto, A. Garcia, Electrochemical corrosion behaviour of a Ti-IF steel and a SAE 1020 steel in a 0.5 M NaCl solution, Mater. Corros. 61 (2010) 407–411, https://doi.org/10.1002/maco.200905420.

[12] H.E. Townsend, Effects of alloying elements on the corrosion of steel in industrial atmospheres, Corrosion 57 (2001) 497–501, https://doi.org/10.5006/1.3290374.

[13] Y. Qian, C. Ma, D. Niu, J. Xu, M. Li, Influence of alloyed chromium on the atmospheric corrosion resistance of weathering steels, Corros. Sci. 74 (2013) 424–429, https://doi.org/10.1016/j.corsci.2013.05.008.

[14] P.K. Katiyar, S. Misra, K. Mondal, Comparative corrosion behavior of five microstructures (pearlite, bainite, spheroidized, martensite, and tempered martensite) made from a high carbon steel, Metall. Mater. Trans. A 50 (2019) 1489–1501, https://doi.org/10.1007/s11661-018-5086-1.

[15] C. Escrivà-Cerdán, S.W. Ooi, G.R. Joshi, R. Morana, H.K.D.H. Bhadeshia, R. Akid, Effect of tempering heat treatment on the CO2 corrosion resistance of quench-hardened Cr-Mo low-alloy steels for oil and gas applications, Corros. Sci. 154 (2019) 36–48.

[16] S. Zhang, Effect of Tempering Temperature on the Corrosion Behavior of R5 Steel in Artificial Seawater, Int. J. Electrochem. Sci. (2017) 2453–2465, https://doi.org/10.20964/2017.03.69.

[17] M. Orłowska, E. Ura-Bińczyk, L. Olejnik, M. Lewandowska, The effect of grain size and grain boundary misorientation on the corrosion resistance of commercially pure aluminium, Corros. Sci. 148 (2019) 57–70, https://doi.org/10.1016/j.corsci.2018.11.035.

[18] J. González, L.-B. Peral, C. Colombo, I. Fernández Pariente, A study on the microstructural evolution of a low alloy steel by different shot peening treatments, Metals (Basel) 8 (2018) 187, https://doi.org/10.3390/met8030187.

[19] L.B. Peral, A. Zafra, S. Bagherifard, M. Guagliano, I. Fernández-Pariente, Effect of warm shot peening treatments on surface properties and corrosion behavior of AZ31 magnesium alloy, Surf. Coat. Technol. 401 (2020), https://doi.org/10.1016/j.surfcoat.2020.126285 126285.

[20] L.B. Peral, A. Quintero, A.T. Vielma, M.F. Barbés, I. Fernández-Pariente, TEM evaluation of steel nanocrystalline surfaces obtained by severe shot peening, Surf. Coat. Technol. 418 (2021), https://doi.org/10.1016/j.surfcoat.2021.127238 127238.

[21] S. Choudhary, V. Nanda, S. Shekhar, A. Garg, K. Mondal, Effect of microstructural anisotropy on the electrochemical behavior of rolled mild steel, J. Mater. Eng. Perform. 26 (2017) 185–194, https://doi.org/10.1007/s11665-016-2465-x.

[22] D. Zhang, X. Gao, G. Su, Z. Liu, N. Yang, L. Du, R.D.K. Misra, Effect of tempered martensite and ferrite/bainite on corrosion behavior of low alloy steel used for flexible pipe exposed to high-temperature brine environment, J. Mater. Eng. Perform. 27 (2018) 4911–4920, https://doi.org/10.1007/s11665-018-3587-0.

[23] M. Qiao, J. Hu, K. Guo, Q. Wang, Influence of shot peening on corrosion behavior of low alloy steel, Mater. Res. Express 7 (1) (2020) 016574.

[24] T. Wang, J. Yu, B. Dong, Surface nanocrystallization induced by shot peening and its effect on corrosion resistance of 1Cr18Ni9Ti stainless steel, Surf. Coat. Technol. 200 (2006) 4777–4781, https://doi.org/10.1016/j.surfcoat.2005.04.046.

[25] C.T. Kwok, F.T. Cheng, H.C. Man, W.H. Ding, Corrosion characteristics of nanostructured layer on 316L stainless steel fabricated by cavitation-annealing, Mater. Lett. 60 (2006) 2419–2422, https://doi.org/10.1016/j.matlet.2006.01.053.

[26] A. Fattah-alhosseini, S. Vafaeian, Comparison of electrochemical behavior between coarse-grained and fine-grained AISI 430 ferritic stainless steel by Mott-Schottky analysis and EIS measurements, J. Alloy. Compd. 639 (2015) 301–307, https://doi.org/10.1016/j.jallcom.2015.03.142.

[27] A.A. Ahmed, M. Mhaede, M. Wollmann, L. Wagner, Effect of surface and bulk plastic deformations on the corrosion resistance and corrosion fatigue performance of AISI 316L, Surf. Coat. Technol. 259 (2014) 448–455, https://doi.org/10.1016/j.surfcoat.2014.10.052.

[28] C. Aparicio, F. Javier Gil, C. Fonseca, M. Barbosa, J.A. Planell, Corrosion behaviour of commercially pure titanium shot blasted with different materials and sizes of shot particles for dental implant applications, Biomaterials 24 (2003) 263–273, https://doi.org/10.1016/S0142-9612(02)00314-9.

[29] P. Wang, L. Ma, X. Cheng, X. Li, Influence of grain refinement on the corrosion behavior of metallic materials: A review, Int. J. Miner. Metall. Mater. 28 (2021) 1112–1126, https://doi.org/10.1007/s12613-021-2308-0.

[30] Q. He, X. Jiang, P. Cai, L. Zhang, T. Sun, X. Yang, K. Zhou, L. Zhang, Effect of Annealing on Microstructure and Corrosion Behavior of Interstitial Free Steel, Materials. 15 (2021) 24, https://doi.org/10.3390/ma15010024.

[31] Metallic materials - Brinell hardness test - Part 1: Test method (ISO 6506-1:2014), (n.d.).

[32] H.M. Rietveld, A profile refinement method for nuclear and magnetic structures, J. Appl. Cryst. 2 (1969) 65–71, https://doi.org/10.1107/S0021889869006558.
[33] G.K. Williamson, W.H. Hall, X-ray line broadening from filed aluminium and wolfram, Acta Metall. 1 (1953) 22–31, https://doi.org/10.1016/0001-6160(53)90006-6.
[34] L.E.A. H.P. Klug, X-ray Diffraction Procedures, 1954.
[35] G.K. Williamson, R.E. Smallman III, Dislocation densities in some annealed and cold-worked metals from measurements on the X-ray debye-scherrer spectrum, Phil. Mag. 1 (1956) 34–46, https://doi.org/10.1080/14786435608238074.
[36] M.N. Yoozbashi, S. Yazdani, XRD and TEM study of bainitic ferrite plate thickness in nanostructured, carbide free bainitic steels, Mater. Chem. Phys. 160 (2015) 148–154, https://doi.org/10.1016/j.matchemphys.2015.03.071.
[37] Geometrical Product Specifications (GPS) - Surface texture: Profile method - Terms, definitions and surface texture parameters - Amendment 1, (n.d.).
[38] Standard Practice for Calculation of Corrosion Rates and Related Information from Electrochemical Measurements 1, n.d.
[39] J.R. Scully, Polarization resistance method for determination of instantaneous corrosion rates, Corrosion 56 (2000) 199–218, https://doi.org/10.5006/1.3280536.
[40] ASTM G106-89 (2015): Standard Practice for Verification of Algorithm and Equipment for Electrochemical Impedance Measurements, (n.d.).
[41] S. Bagherifard, D.J. Hickey, S. Fintová, F. Pastorek, I. Fernandez-Pariente, M. Bandini, T.J. Webster, M. Guagliano, Effects of nanofeatures induced by severe shot peening (SSP) on mechanical, corrosion and cytocompatibility properties of magnesium alloy AZ31, Acta Biomater. 66 (2018) 93–108, https://doi.org/10.1016/j.actbio.2017.11.032.
[42] S. Bagherifard, I. Fernandez-Pariente, R. Ghelichi, M. Guagliano, Severe Shot Peening to Obtain Nanostructured Surfaces: Process and Properties of the Treated Surfaces, in: Handbook of Mechanical Nanostructuring, Wiley-VCH Verlag GmbH & Co. KGaA, Weinheim, Germany, 2015, pp. 299–323, https://doi.org/10.1002/9783527674947.ch14.
[43] SAE J443 (2013): Procedures for using standard shot peening test strip, (n.d.).
[44] A NATIONAL MEASUREMENT GOOD PRACTICE GUIDE Determination of Residual Stresses by X-ray Diffraction-Issue 2, n.d.
[45] I. Fernández Pariente, M. Guagliano, About the role of residual stresses and surface work hardening on fatigue ΔKth of a nitrided and shot peened low-alloy steel, Surf. Coat. Technol. 202 (2008) 3072–3080, https://doi.org/10.1016/j.surfcoat.2007.11.015.
[46] ASTM E92-17: Standard Test Methods for Vickers Hardness and Knoop Hardness of Metallic Materials, (n.d.).
[47] B. Evgeny, T. Hughes, D. Eskin, Effect of surface roughness on corrosion behaviour of low carbon steel in inhibited 4 M hydrochloric acid under laminar and turbulent flow conditions, Corros. Sci. 103 (2016) 196–205, https://doi.org/10.1016/j.corsci.2015.11.019.
[48] T. Maki, Morphology and substructure of martensite in steels, in: Phase Transformations in Steels, Elsevier, 2012, pp. 34–58, https://doi.org/10.1533/9780857096111.1.34.
[49] B.D. (Bernard D. Cullity, Elements of x-ray diffraction, Addison-Wesley Publishing Company, Inc, 1978.
[50] E. Remita, B. Tribollet, E. Sutter, V. Vivier, F. Ropital, J. Kittel, Hydrogen evolution in aqueous solutions containing dissolved CO2: Quantitative contribution of the buffering effect, Corros. Sci. 50 (2008) 1433–1440, https://doi.org/10.1016/j.corsci.2007.12.007.
[51] Y. Lu, H. Jing, Y. Han, L. Xu, Effect of temperature on the 3Cr low-alloyed steel initial corrosion behavior in CO2 solution, Mater. Chem. Phys. 178 (2016) 160–172, https://doi.org/10.1016/j.matchemphys.2016.04.083.
[52] P.K. Katiyar, S. Misra, K. Mondal, Corrosion behavior of annealed steels with different carbon contents (0.002, 0.17, 0.43 and 0.7% C) in freely aerated 3.5% NaCl solution, J. Mater. Eng. Perform. 28 (2019) 4041–4052, https://doi.org/10.1007/s11665-019-04137-5.
[53] W. Liu, Q. Zhou, L. Li, Z. Wu, F. Cao, Z. Gao, Effect of alloy element on corrosion behavior of the huge crude oil storage tank steel in seawater, J. Alloy. Compd. 598 (2014) 198–204, https://doi.org/10.1016/j.jallcom.2014.01.181.
[54] B. Hirschorn, M.E. Orazem, B. Tribollet, V. Vivier, I. Frateur, M. Musiani, Determination of effective capacitance and film thickness from constant-phase-element parameters, Electrochim. Acta 55 (2010) 6218–6227, https://doi.org/10.1016/j.electacta.2009.10.065.
[55] B. Kinsella, Y.J. Tan, S. Bailey, Electrochemical impedance spectroscopy and surface characterization techniques to study carbon dioxide corrosion product scales, Corrosion 54 (1998) 835–842, https://doi.org/10.5006/1.3284803.
[56] S.P. Sah, Corrosion of 304 stainless steel in carbonates melt– a state of enhanced dissolution of corrosion products, Corros. Sci. 169 (2020) 108535.
[57] K.S. Cole, R.H. Cole, Dispersion and absorption in dielectrics I. Alternating current characteristics, J. Chem. Phys. 9 (1941) 341–351, https://doi.org/10.1063/1.1750906.
[58] D. Dwivedi, K. Lepková, T. Becker, Carbon steel corrosion: a review of key surface properties and characterization methods, RSC Adv. 7 (2017) 4580–4610, https://doi.org/10.1039/C6RA25094G.
[59] H.J. Cleary, N.D. Greene, Corrosion properties of iron and steel, Corros. Sci. 7 (1967) 821–831, https://doi.org/10.1016/S0010-938X(67)80115-X.
[60] L.Q. Guo, M. Li, X.L. Shi, Y. Yan, X.Y. Li, L.J. Qiao, Effect of annealing temperature on the corrosion behavior of duplex stainless steel studied by in situ techniques, Corros. Sci. 53 (2011) 3733–3741, https://doi.org/10.1016/j.corsci.2011.07.019.
[61] J. Jiang, Y. Liu, H. Chu, D. Wang, H. Ma, W. Sun, Pitting corrosion behaviour of new corrosion-resistant reinforcement bars in chloride-containing concrete pore solution, Materials. 10 (2017) 903, https://doi.org/10.3390/ma10080903.
[62] J. Stewart, D.E. Williams, The initiation of pitting corrosion on austenitic stainless steel: on the role and importance of sulphide inclusions, Corros. Sci. 33 (1992) 457–474, https://doi.org/10.1016/0010-938X(92)90074-D.